Silicon nanocrystal photovoltaic device fabricated via photolithography and its current–voltage temperature dependence

Lingfeng Wu *, Tian Zhang, Ziyun Lin, Xuguang Jia, Binesh Puthen-Veettil, Terry Chien-Jen Yang, Hongze Xia, Gavin Conibeer, Ivan Perez-Wurfl

Australian Centre for Advanced Photovoltaics, School of Photovoltaic and Renewable Energy Engineering, TETB Building (H6), The University of New South Wales, Kensington, NSW 2033, Australia

ABSTRACT

Photolithography is used as an alternative method to overcome the challenge of making anode and cathode contacts on a Si nanocrystal solar cell deposited on non-conductive substrates instead of reactive ion etching (RIE). The advantages of this method include better control of isolation mesa fabrication and the avoidance of device exposure to highly energetic particles which may cause unpredictable damage. The photovoltaic device fabricated shows an open-circuit voltage (V_{OC}) and a short-circuit current density (J_{SC}) of 270 mV and 0.124 mA/cm^2 respectively at room temperature under one-sun illumination. Current–voltage measurements were performed at temperatures (T) from 77 K to 300 K. A model that includes recombination-generation current in the depletion region is considered to explain the observed current behaviour of the device. An ideality factor very close to 2 was calculated based on Suns-V_{OC} measurement, which indicates that the device is limited by recombination in the depletion region. A discrepancy was observed between the peaks (1.47 eV) in the photoluminescence spectrum and maximum V_{OC} (0.81 V) extrapolated from the V_{OC}–T relation at 0 K. This discrepancy has been attributed to the temperature dependence of the carrier lifetime in the depletion region characterized by an activation energy later defined in this article.

© 2014 Elsevier B.V. All rights reserved.

1. Introduction

A tandem solar cell structure made using materials with different bandgaps is an effective way to reduce thermalisation losses. Due to the effect of quantum confinement, wide bandgap low dimensional structures can be fabricated with current nano-fabrication techniques. It is therefore, in principle, possible to make a solar cell with tunable bandgaps using primarily Si [1]. In the standard fabrication technique used in this work, crystallisation of Si nanocrystals occurs at temperatures > 1000 °C, narrowing the range of candidates that could be used as conductive substrates. As reliable conductive substrates for Si nanocrystal (NC) material are still under investigation, finding a substrate to make low-resistivity ohmic contact on either n- and p-type layers remains challenging. To overcome this problem, a "mesa structure" is used where the anode and cathode contacts are made on the same side of the device [2]. Reactive ion etching (RIE) is then required for the fabrication process to make these mesas on p–i–n Si nanocrystal thin films. However, RIE is likely to

have a negative impact on device performance as the p–n junction is directly exposed to highly energetic particles. The p–n junction is a crucial part of a solar cell and even minor damage on the edge of this junction can cause significant degradation in its performance [3]. In addition, the etching rate is not easy to control as the Si-NC material is embedded in an oxide or nitride matrix which may have a very different etch rate compared to the Si-NC. The rate difference can cause a significant level of surface roughness on the thin-film material. In this work, an alternative method of fabrication avoiding the use of RIE is introduced. Instead of RIE, photolithography was applied to facilitate the making of mesas on the thin films. The p-type thin film was deposited first by reactive ion sputtering on a quartz substrate. We will call this layer the "bottom layer" of the device throughout this article. Photolithography was then employed to define mesas on the top of this bottom layer. Openings in photoresist were made to expose areas intended to become diodes. The rest of the area, still covered by the photoresist, allows contacts to be placed on the bottom layer. Intrinsic and n-type materials were then deposited to cover the surface of the mesa. A subsequent lift-off defined the i–n active areas. In spite of more fabrication steps in the photolithography method, they are comparatively more controllable and less likely

to cause rough thin-film surface. Afterwards, annealing of the Si-NC material was followed by metallization and contact sintering to fabricate a working device. Suns-V_{OC} was employed to determine the ideality factor of the device. Current–Voltage relations at temperatures from 77 K to 300 K with and without illumination were obtained. Discussion of the I–V characteristics and bandgap analysis will follow. This work points out that the electrical performance of the Si nanocrystal solar cell may be limited by Shockley–Read–Hall recombination in its depletion region. Further improvement of similar devices should focus on reducing trapping states in the depletion region.

2. Material and methods

The thin-film material used in this work was deposited via RF sputtering onto quartz substrates in an argon atmosphere at a pressure of 1.5×10^{-3} Torr using a computer controlled AJA ATC-2200 sputtering system. 4-inch Si and SiO_2 targets and a 2-inch boron target were used for Si rich oxide (SRO) and dielectric deposition and for doping respectively. Before sputtering, the chamber was evacuated to a base pressure of at least 3×10^{-7} Torr. These sputtered thin-films on quartz substrates contained alternating layers of SRO and silicon dioxide (SiO_2). The thickness of each SiO_2 and SRO layer was 1.8 nm and 4 nm respectively.

The "unit-structure" made of a SRO layer and a SiO_2 layer with the former layer deposited on top of the latter will be addressed as a "bi-layer". The volume ratio of Si in the SRO layer, expressed as a percentage, is defined as the ratio between the deposition rate (nm/min) of Si and the sum of the deposition rate of Si and SiO_2. The deposition rate was calculated based on the thickness of either SiO_2 or SRO layer deposited over a certain time period measured with a Woollam VASE FQ-TH100 ellipsometer. The thickness determined with this method was verified by comparing to the value determined using X-ray reflectivity. The discrepancy between the two methods was $\pm 4.2\%$. The co-sputtered samples reported in this work had volume ratios at 55%, 60% and 66% by adjusting the sputtering power of the Si target while keeping the power for the SiO_2 target fixed. SRO layers were doped with B during sputtering where the boron RF power source was set to supply 34 W power to the sputtering gun. The number of bilayers deposited was 30. A 20 nm capping layer made of SiO_2 was deposited on the surface of each sample as a protective layer. After the deposition, the samples were annealed in a N_2-purged tube furnace at 1100 °C for 1 h to facilitate Si QD nucleation and growth.

After these B-doped alternating SRO/SiO_2 thin-films had been annealed, negative photoresist nLOF2020 was employed to define mesas on the film. The nLOF2020 photoresist was spun at a speed of 3000 rpm for 30 s and then prebaked at 110 °C for 1 min. The resist was then exposed for 4 s using a Quintel 6000 mask aligner equipped with an UV light source (365 nm) with a measured 10 mW/cm² intensity. The resist was post baked at 110 °C for 1 min and subsequently submerged in AS826MIF developer for 65 s to fully remove the unexposed photoresist. At this stage, the mesa areas on the thin-films could be clearly observed (Fig. 1a). These openings as shown in Fig. 1a became windows for subsequent SiO_2/SRO bilayer deposition. To remove undesired photoresist residue and other possible organic contaminants, the samples were cleaned in a Denton O_2 plasma asher at an O_2 pressure of 340 mTorr for 20 min. To further remove possible residue on the B-doped thin-films and hence to expose the underlying B-doped bilayer, the protective oxide capping layer was removed by hydrofluoric acid immediately before loading into the load lock of the sputtering tool. Undoped and phosphine-doped SRO/SiO_2

materials were then deposited following a similar sputtering process. A combination of Ar and PH_3 (99:1) was injected into the sputtering chamber at a flow rate at 3 sccm during PH_3-doped-SRO/SiO_2 material deposition.

When the second AJA deposition was finished, the nLOF2020 photoresist was removed using N-Methyl-2-Pyrrolidone (NMP) to define the mesas by liftoff (Fig. 1b). Then the SRO thin film was annealed at 1100 °C for 1 h again to achieve the Si nanocrystal formation in the undoped and PH_3-doped thin-films. Metal contact deposition was also achieved via a liftoff process on both the n and p-type Si NC thin film contact areas by using positive photoresist AZ6612. A mask designed to make openings on both bottom and top (undoped followed by PH_3-doped-bilayered thin films) layers was used during UV exposure. In the metallization process, similar to the previous SRO deposition, the aluminium contacts were defined via lift-off to complete the full structure of a photovoltaic device (Fig. 1c).

The thin-film materials investigated had 55%, 60% and 66% Si by volume (Si:SRO). Apart from this difference they shared a similar structure—30 B-doped bilayers, followed by 10 undoped bilayers and 30 PH_3-doped bilayers. Each bilayer is made of 1.8 nm SiO_2 and 4 nm SRO. SiO_2 layers were not doped during sputtering. Metal contacts were deposited on the top of B-doped thin-films and PH_3-doped thin-films respectively to make the devices available for electrical measurement.

3. Results and discussion

3.1. Current–voltage relation

The photovoltaic device with Si volume ratio of 66% in the SRO layers showed an open circuit voltage (V_{OC}) of 270 meV and a short circuit current density (J_{SC}) of 0.124 mA/cm² at 25 °C under 1-sun illumination. The current density is calculated based on the area of the mesa (overlapping region of p- and i-type bilayers). The Fill Factor of this device is 0.277. In contrast, I–V measurements on devices prepared with SRO volume ratios of 60% and 55% were not measurable. It is suspected that the comparatively low Si content leads to a very high resistivity which impedes the flow of current to such an extent that it is not measurable. An optimised Si percentage for photovoltaic purpose should be found for future fabrication of Si NC solar cells. The average size depends greatly on the stoichiometry of the SiO_X as pointed out by reference [4]. When the Si content is increased, the average size of Si NCs will generally be larger. According to the effective mass theory [5], the effective bandgap of the material will hence become lower. To ensure the effect of quantum confinement to a certain extent, a sufficiently low Si content in the device should be chosen. The Fill Factor and efficiency of the device are low probably due to the high resistivity and low V_{OC}. Therefore the primary challenge of such devices may be to improve the V_{OC}. According to our current results, the optimal ratio might be higher than 60% and could be around 66%. Both "illuminated" and "dark" I–V curves are shown in Fig. 2.

Transmission line measurements (TLM) showed a linear current–voltage relation between contacts both on the top and the bottom layers. The sheet resistance was measured at different temperatures using the circular transmission line method (CTLM). At 300 K, the sheet resistance of the bottom layer was $3.03 \times 10^7 \, \Omega/sq$ ($\pm 1.77\%$), while the sheet resistance measured on the top layer of the device was $7.65 \times 10^5 \, \Omega/sq$ ($\pm 1.74\%$). Here we used a method introduced in the literature to calculate the external series resistance of the device based on the mesa's geometry defined in Ref. [2]. It is defined as an external resistance because it does not include the resistance due to internal effects
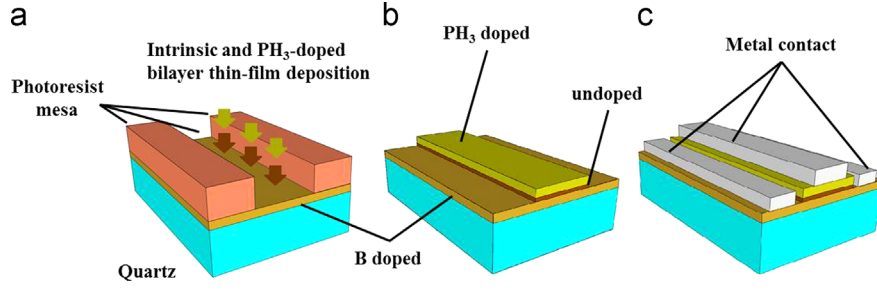
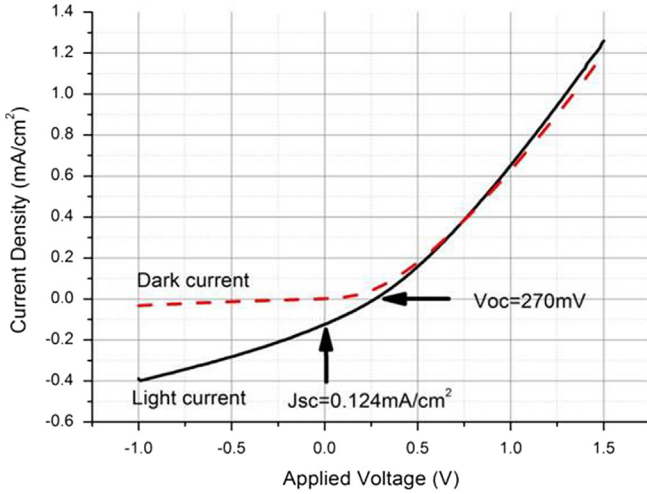**Fig. 1.** The fabrication process of photovoltaic device by using photolithography.

Fig. 2. Current–voltage relation (I–V curve) of photovoltaic device with 66% Si in the SRO layers. Straight line shown corresponds to the illuminated (one sun) I–V while the dash line corresponds to the dark I–V.

Table 1
Redefined external series resistance calculated based on mesa geometry.

Temperature (K)	Redefined series resistance (10^2 Ω cm^2)
77	80.5
100	28.5
125	17.8
150	10.4
175	6.3
200	4.5
225	3.2
250	2.3
275	1.8
300	1.2

such as current crowding. It is given by

$$R_{\text{ext}}(T) = \frac{R_{\text{sheet}}(T)W_a}{2L} + \frac{R_{\text{cont}}(T)}{2L} \tag{1}$$

where the $R_{\text{sheet}}(T)$ in Ω/sq is the measured sheet resistance of the bottom layer (B doped layer) at a certain temperature T calculated based on TLM, W_a is the distance (5 µm) the current flows laterally in the bottom layer before reaching the edge of the mesa, L is the total length of the contact in cm and $R_{\text{cont}}(T)$ is the contact resistance in $\Omega \cdot$cm. The contact resistance could also be calculated based on TLM. The external series resistance will be redefined according to the unit cell area since the current density will be discussed instead of current. The redefined series resistance for this specific device ($R_{\text{ext}} \times$ unit cell area) is shown in Table 1. The shunt resistance was extracted from the slope of the I–V curve within the range 0 to -0.1 V. I–V curves with the external parasitic effect removed can be obtained and are presented in Fig. 3.

Temperature dependent I–V curves shown in Fig. 3b demonstrate an increase in the reverse diode current as the temperature rises. They did not saturate at a particular level as would be expected for an ideal diode but instead behaved super-linearly with an increasing reverse bias voltage. Generally, if a diode's reverse current is dominated by diffusion current due to recombination in the quasi-neutral region, the current at a sufficiently high reverse bias approaches the saturation current. In this work, however, the reverse current observed seems to be dominated by another mechanism. It could instead be a result of carrier generation in the depletion region [6]. Assuming that Shockley–Read–Hall (SRH) recombination was the dominant recombination mechanism in this diode, a reduction of carrier concentrations under reverse bias ($pn \ll n_i^2$) leads to a higher carrier generation

rate than recombination rate. This gives rise to a simplified version of SRH recombination expression as pointed out in Ref. [7]

$$U = -\left[\frac{\sigma_n \sigma_p v_{\text{th}} N_t}{\sigma_n \exp((E_t - E_i)/kT) + \sigma_p \exp((E_i - E_t)/kT)}\right] n_i \equiv -\frac{n_i}{\tau_D} \tag{2}$$

where E_t stands for trapping state energy level, σ_n and σ_p are the capture cross-section areas for electrons and holes respectively, E_i is the intrinsic Fermi energy level, v_{th} is the thermal velocity and N_t is the trapping state density, the τ_D is the carrier generation lifetime, defined as the reciprocal of the term in the brackets. The generation current can therefore be written as follows, assuming that the generation rate is constant throughout the depletion region.

$$J_{\text{reverse}} \approx J_{\text{gen}} \approx \frac{qn_i W_D}{\tau_D} \tag{3}$$

where W_D stands for the width of the depletion region. The intrinsic carrier density increases with increasing temperature. Mathur et al. point to the lifetime decreasing exponentially with increasing $1/T$ [8]. In general, the combined effect is that the generation current J_{gen} goes up when temperature rises. The quantitative reason will be given in Section 3.2 as to why n_i/τ_D still increases with an increasing temperature. A reverse current that does not saturate can be observed when it is dominated by this generation current. Also, as pointed by out in Sze et al. [7], the width W_D of the depletion region increases as the reverse bias goes up. This increasing width W_D would lead to an increasing generation current, which is consistent with the measured I–V relation shown in Fig. 3b.

The semi-log plot of dark I–V curve under forward bias shows an obvious changing slope throughout the forward bias voltage range as shown in Fig. 3a. The region dominated by the diode characteristics was difficult to observe in these curves, where recombination occurring in the depletion region and internal parasitic resistance impacts heavily on the performance of the device [2]. This internal parasitic effect can be due to current crowding, which is current dependent.
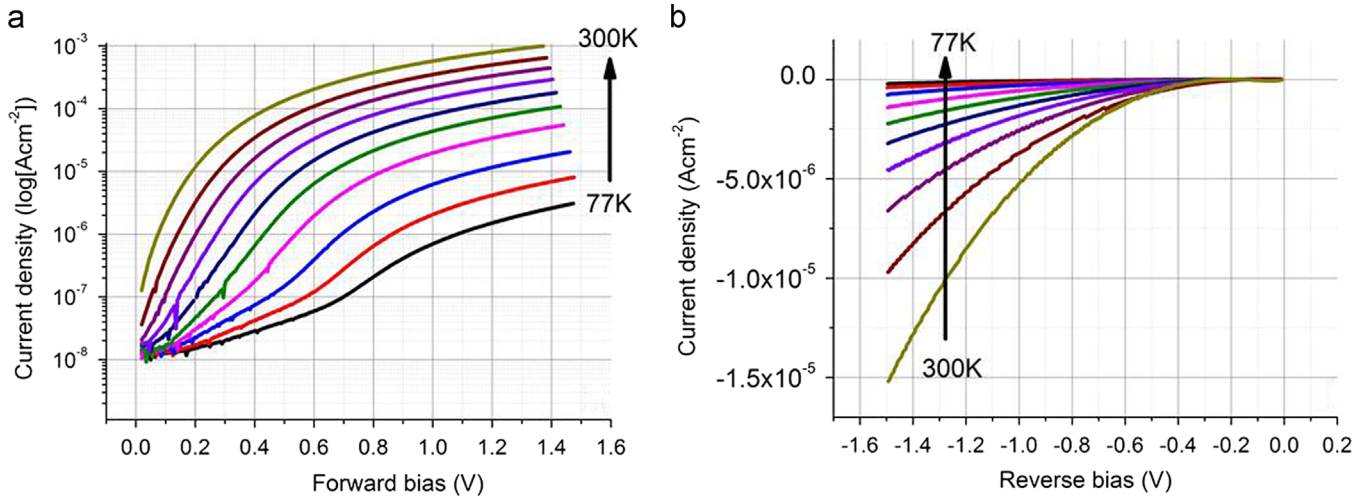
Fig. 3. Semi-log plot of dark *I–V* curves under bias from 77 K to 300 K (a) dark *I–V* observed in forward bias region (b) dark *I–V* observed in reverse bias region.

3.2. Bandgap investigation

Since it was difficult to remove the internal parasitic effect in this case, Suns-V_{OC} was employed to calculate the ideality factor of the device. The ideality factor is given by

$$n = \frac{q(V_{oc2} - V_{oc1})}{kT \ln(Jsc2_{reference}/Jsc1_{reference})} \quad (4)$$

where the V_{oc1} and V_{oc2} are the V_{OC} of the device measured at different intensities 1 and 2, k is the Boltzmann constant, T is the temperature, $Jsc1_{reference}$ and $Jsc2_{reference}$ are the short-circuit current densities of the reference diode measured at intensities 1 and 2. Effectively, this current is proportional to the light intensity. From Fig. 4 we can see the calculated ideality factor remains very close to 2 in the range of V_{OC} from 0.15 V to 0.38 V at room temperature. This happens when the forward current is limited by the recombination current in the depletion region. This was consistent with the generation current from the same region observed above.

The ideality factor indicates that the contribution of recombination in the quasi-neutral region is small compared to that arising from recombination in the depletion region. Hence the expression of the dark saturation current can be written including only the diode current due to the recombination in the depletion region. It is given by [7]

$$J_o \approx \sqrt{\frac{\pi}{2}} \frac{kT}{E_o} \frac{n_i}{\tau_D} = \frac{\sqrt{\pi N_C N_V/2}(kT/E_o)\exp(-(E_g/2kT))}{\tau_D} = A \frac{\exp(-(E_g/2kT))}{\tau_D} \quad (5)$$

and

$$A = \sqrt{\frac{\pi N_C N_V}{2}} \frac{kT}{E_o} \quad (5.1)$$

where E_o is the electric field at the location of maximum recombination, τ_D is the carrier recombination lifetime in the depletion region, and E_g is the effective bandgap of this NC material.

The photoluminescence spectrum shown in Fig. 5 was obtained using a 405 nm violet–blue laser. A peak in the spectrum was located at 1.47 eV as shown in Fig. 5, which is consistent with previous results [4,9]. The peak position of the PL spectrum obtained in this bilayer structure indicates that the 1.8 nm SiO_2 layers are able to restrict the growth of the nanocrystals. Considering that this peak is observed at an energy consisted with 3–4 nm Si nanocrystals, we believe the thinner SiO_2 barrier is
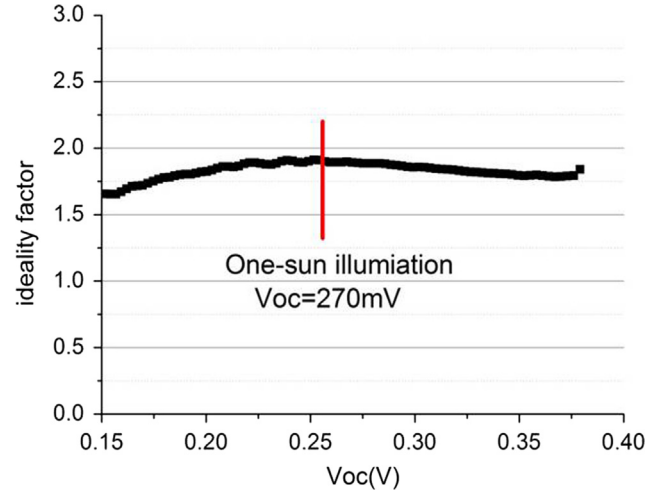

Fig. 4. The relation between calculated ideality factor and V_{OC}. The ideality factor remains close to 2 within the observed range V_{OC}=0.15–0.38 V.
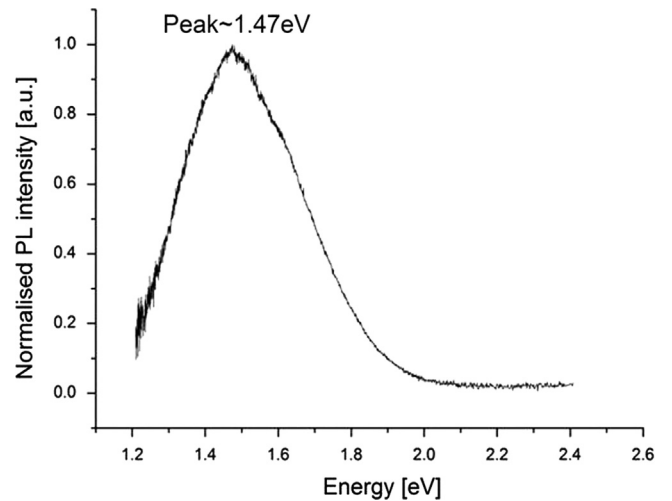

Fig. 5. Photoluminescence spectrum from diode with Si volume ratio at 66%.

able to maintain the nanocrystals spatially separated. Plotting the temperature dependence of the measured V_{OC}, it can be found that the V_{OC} increases linearly as the temperature drops from 300 K to 77 K as shown in Fig. 6. The extrapolated intercepts of V_{OC}–T
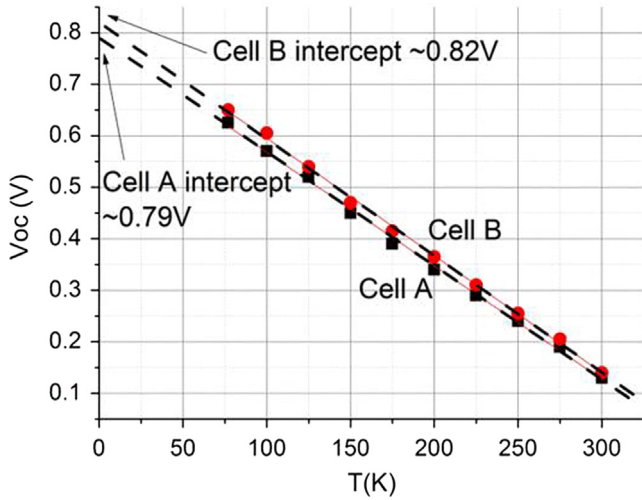
Fig. 6. Open-circuit voltage measured under constant tungsten halogen light illumination conditions at different temperatures and its intercept on the voltage axis.

relation at $T=0$ K are 790 mV and 820 mV for devices A and B respectively. Both devices A and B share the same structure and Si volume ratio of 66%. The voltage difference between these two devices could be due to the variation in metallization and non-uniformity of gas flow during contact sintering. Though it is difficult to measure the actual positions of the quasi-Fermi levels directly, the maximum split of these levels can be determined by extrapolating the V_{OC}–T relation at $T=0$ K under illumination. At 0 K, there should be no thermally generated carriers in the device but excess carriers generated by illumination. At this temperature, ideally any increase in the carrier concentration due to photo-generated carriers would cause the quasi-Fermi levels to coincide with the band edges, regardless of the illumination intensity. However, to be able to extrapolate the measured V_{OC} to $T=0$ K, a constant illumination condition should be maintained at all temperatures as the logarithm of the photocurrent determines the rate (slope) at which V_{OC} approaches the bandgap as the temperature decreases (see Eq. (6)). Here we define the elementary charge multiplied by V_{OC} extrapolated to $T=0$ K as the electronic bandgap (EBG) of the device. As pointed out in previous work [10], this EBG reflects the magnitude of the material bandgap E_g based on the maximum splitting of quasi-Fermi energy levels of electrons and holes. Based on Eq. (5) the V_{OC} for these devices can be express as follow:

$$qV_{OC} \approx nkT \ln\left(\frac{J_{SC}}{J_o}\right) = 2kT \ln\left(\frac{J_{sc}\tau_D}{A}\right) + E_g \tag{6}$$

It has been reported that the location of the PL peak in the energy domain matches the effective bandgap obtained by the effective mass theory [5], which can be expressed by $E_g = E_{gbulk} + (C/d^2)$, where E_{gbulk} is the bandgap of bulk crystal Si, C is the confinement parameter and d is the dimension of Si nanocrystals. We assume that the PL peak indicates the effective bandgap of the device. If an average value of the measured EBG is taken as 805 meV, we can see that it is 665 meV lower than the PL peak. Such a discrepancy is not negligible and can reveal information hidden behind the limiting recombination mechanism in each characterization technique used. Since the device's electrical performance is limited by the SRH recombination in the depletion region, the device performance follows Eq. (6) shown above. Photoluminescence, on the contrary, is the result of band-to-band recombination in the material. The peak energy in the PL spectrum measures the bandgap for band-to-band recombination,

while the EBG results from the combined effects of SRH recombination and the magnitude of the effective bandgap plus a small offset of the order of 3kT. These combined effects are contained within the lifetime τ_D. Eq. (6) shows that the extracted EBG may be equal to E_g if τ_D is only weakly dependent on temperature. However, in materials with many interfaces such as polycrystalline Si, the carrier lifetime has an exponential dependence on the reciprocal of temperature, with activation energy due to the grain boundary barrier potential as reported in Ref. [8]. With this in mind, it is then easy to associate the lifetime in Eq. (6) with an activation energy due to interface potential barriers and states in the nanocrystal material. Eq. (6) can then be rewritten with this assumption

$$\tau_D = \tau_o \exp\left(-\frac{E_{AL}}{kT}\right) \tag{7}$$

where E_{AL} is the activation energy of the minority carrier recombination lifetime in the depletion region. If we substitute (7) with τ_D from Eq. (6), it becomes

$$qV_{OC} = 2kT \ln\left(\frac{J_{SC}\tau_o}{A}\right) + E_g - 2E_{AL} \tag{8}$$

It is known from Eq. (8) that the EBL extracted above is $(E_g - 2E_{AL})$, with an offset of $2E_{AL}$ from E_g. The lifetime activation energy E_{AL} is equal to 332 meV in this specific case. With the result here that the temperature dependence of the minority carrier recombination lifetime in the depletion region is given by

$$\tau_D = \tau_o \exp\left(-\frac{332\text{ meV}}{kT}\right) \tag{9}$$

This model explains why the extracted electronic bandgap is not equal to the observed PL peak in a device limited by recombination in the depletion region. Since V_{OC} is limited by SRH recombination, the offset can be described by a physical model where the trapping states in the depletion region suppress the splitting of quasi-Fermi energy levels. The calculated value 332 meV of the lifetime activation energy indicates that τ_D changes to a lesser extent than n_i, with an activation energy of half of the bandgap (about 740 meV calculated based on PL peak location). Hence n_i/τ_D rises with an increase in temperature. Thus this explains the observed behaviour in Section 3.1 where the generation current J_{gen} goes up with an increase in temperature according to Eq. (3). Eq. (8) indicates that the V_{OC} of the device may be increased by reducing the activation energy of lifetime or increasing the lifetime pre-factor τ_o. A more in depth study would be required to investigate the recombination mechanism in this material.

4. Conclusions

We report an alternative method to fabricate lateral-structured Si nanocrystal (NC) solar cells by using photolithography, instead of RIE. With the help of photolithography, the fabrication is more reliable and the unpredictable damage induced by RIE can be avoided. Temperature-dependent electrical properties of the photovoltaic device were investigated. After the calculated external series resistance based on the mesa's geometry was removed, a current density increasing superlinearly with reverse bias voltage was observed. We attribute this behaviour to a carrier recombination-generation mechanism in the depletion region based on the Shockley–Read–Hall (SRH) model. The reverse current increases as temperature increases due to a short generation lifetime in the depletion region. Suns-V_{OC} measurements confirmed that the device was limited by recombination in the depletion region. The photoluminescence spectrum from the device showed a peak at 1.47 eV. The maximum

V_{OC} (at 0 K) extrapolated from the V_{OC}–T relation was about 0.81 V which we defined as the electronic bandgap. Ideally, both the photoluminescence peak and electronic bandgap were expected to reveal the magnitude of the effective bandgap. A possible reason for the discrepancy between them was discussed. It was proposed that the difference is due to the recombination mechanism being different in PL and in the V_{OC}–T measurement. The electrical properties of the device are limited by SRH recombination, while PL is limited by band-to-band recombination. The key factor is the existence of a large activation energy for the minority carrier recombination lifetime. In the SRH-recombination-limited scenario, the lifetime increased exponentially with temperature, with a corresponding activation energy describing the increase rate. Twice this activation energy is then subtracted from the electronic bandgap resulting in a smaller bandgap being extracted from the V_{OC}–T measurements. This study outlines the important role of SRH recombination in the device's electrical performance when the activation energy of the lifetime cannot be ignored. It also suggests that SRH recombination in the depletion region would need to be reduced to further improve the electrical performance of nanocrystal solar cells.

Acknowledgement

References

[1] G. Conibeer, M. Green, E.-C. Cho, D. König, Y.-H. Cho, T. Fangsuwannarak, G. Scardera, E. Pink, Y. Huang, T. Puzzer, S. Huang, D. Song, C. Flynn, S. Park, X. Hao, D. Mansfield, Silicon quantum dot nanostructures for tandem photovoltaic cells, Thin Solid Films 516 (20) (2008) 6748–6756.

[2] I. Perez-Wurfl, X. Hao, A. Gentle, D.-H. Kim, G. Conibeer, M.A. Green, Si nanocrystal p–i–n diodes fabricated on quartz substrates for third generation solar cell applications, Appl. Phys.Lett. 95 (15) (2009) 153506-1–153506-3.

[3] M. Takahashi, T. Shishido, H. Iwasa, H. Kobayashi, Passivation of defect states in surface and edge regions on pn-junction Si solar cells by use of hydrogen cyanide solutions, Cent. Eur. J. Phys. 7 (2) (2009) 227–231.

[4] M. Zacharias, J. Heitmann, R. Scholz, U. Kahler, M. Schmidt, J. Blasing, Size-controlled highly luminescent silicon nanocrystals: a SiO/SiO2 superlattice approach, Appl. Phys. Lett. 80 (4) (2002) 661–663.

[5] T.-Y. Kim, N.-M. Park, K.-H. Kim, G.Y. Sung, Y.-W. Ok, T.-Y. Seong, C.-J. Choi, Quantum confinement effect of silicon nanocrystals in situ grown in silicon nitride films, Appl. Phys. Lett. 85 (22) (2004) 5355–5357.

[6] E.M. Pell, Reverse current and carrier lifetime as a function of temperature in germanium junction diodes, J. Appl. Phys. 26 (6) (1955) 658.

[7] S.M. Sze, K.K. Ng, Physics of Semiconductor Devices, Wiley, 2006, ISBN: 978-0-471-14323-9.

[8] P.C. Mathur, R.P. Sharma, P. Saxena, J.D. Arora, Temperature dependence of minority carrier lifetime in single-crystal and polycrystalline Si solar cells, J. Appl. Phys. 52 (5) (1981) 3651–3654.

[9] D. Di, I. Perez-Wurfl, A. Gentle, D.H. Kim, X. Hao, L. Shi, G. Conibeer, M.A. Green, Impacts of post-metallisation processes on the electrical and photovoltaic properties of Si quantum dot solar cells, Nanoscale Res. Lett. 5 (11) (2010) 1762–1767.

[10] U. Rau, H.W. Schock, Electronic properties of Cu(In,Ga)Se2 heterojunction solar cells–recent achievements, current understanding, and future challenges, Appl. Phys. A 69 (2) (1999) 131–147.